Soft tissue monitoring of the surgical field: detection and tracking of breast surface deformations

Winona L. Richey, Jon S. Heiselman, Morgan J. Ringel, Ingrid. M. Meszoely, Michael I. Miga

Abstract— Objective: **Deformable object tracking is common in the computer vision field, with applications typically focusing on nonrigid shape detection and usually not requiring specific 3D point localization. In surgical guidance however, accurate navigation is intrinsically linked to precise correspondence of tissue structure. This work presents a contactless, automated fiducial acquisition method using stereo video of the operating field to provide reliable fiducial localization for an image guidance framework in breast conserving surgery.** *Methods:* **On *n=8* breasts from healthy volunteers, the breast surface was measured throughout the full range of arm motion in a supine mock-surgical position. Using hand-drawn inked fiducials, adaptive thresholding, and KAZE feature matching, precise three-dimensional fiducial locations were detected and tracked through tool interference, partial and complete marker occlusions, significant displacements and nonrigid shape distortions.** *Results:* **Compared to digitization with a conventional optically tracked stylus, fiducials were automatically localized with 1.6 ± 0.5 mm accuracy and the two measurement methods did not significantly differ. The algorithm provided an average false discovery rate <0.1% with all cases' rates below 0.2%. On average, 85.6 ± 5.9% of visible fiducials were automatically detected and tracked, and 99.1 ± 1.1% of frames provided only true positive fiducial measurements, which indicates the algorithm achieves a data stream that can be used for reliable on-line registration.** *Conclusions:* **Tracking is robust to occlusions, displacements, and most shape distortions.** *Significance:* **This work-flow friendly data collection method provides highly accurate and precise three-dimensional surface data to drive an image guidance system for breast conserving surgery.**

Keywords—**breast, surgery, lumpectomy, computer vision, fiducial markers, image guidance, localization, marker design, soft tissue deformation**.

I. INTRODUCTION

COMPUTER vision has been increasingly utilized in surgery for a wide variety of applications ranging from understanding surgical process to computer aided detection and navigation [1]. While its use in tool tracking has been a key component in standard-of-care guidance systems for decades, computer vision methods for soft tissue tracking have had more limited development. Several recent surgical technologies have utilized unique printed markers (e.g. ArUco [2] or ARTag [3] fiducials) to localize skin surface information during surgical procedures [4-6]. However, even in rigid scenarios, localization errors for these types of fiducials can be high. In a study comparing 12 common marker dictionaries, localization error was over 7 mm on average for 0-75° viewing angles. Though two methods achieved accuracy suitable for surgical applications (below 2 mm), results are reported for relatively large tags (5 cm) mounted onto rigid, planar boards and viewed from close distances (0.05-0.5 m) [7]. Commercial systems for computer vision tracking of rigid tools, such as the Claronav MicronTracker, report 0.2 mm calibration accuracy from 0.4-1.0 m distances, though viewing angles and lighting conditions are not reported [8].

While many vision-based toolkits for tracking markers are freely available and easily adoptable, their accuracy is limited [9], especially in the context of the dynamic surgical environment. These tags are designed to be mounted on rigid, planar surfaces. These rigid assumptions result in reduced detection rate and accuracy when fixed to nonrigid surfaces, such as skin in deforming surgical applications. Recently, a marker detection system has been proposed using deformable fiducial tags [10], but surgical use would still rely on a cumbersome process of printing and mounting specialized, large, and obstructive tags to skin in the sterile operating environment. Furthermore, in the context of image guidance systems, each point's correspondence to its preoperative imaging counterpart is essential. When using these tag-based approaches, this correspondence is not intuitive to users because the marker patterns have no immediate relationship to the imaging data.

The work herein presents a fiducial detection and tracking algorithm customized for surgical guidance applications with intuitive ink-based alphabetic labels hand drawn directly onto the skin surface. These letter-based fiducials enable three-dimensional (3D) point measurements during surgery, so that information rich preoperative images can be aligned with the patient on the operating room (OR) table, enhancing surgeon understanding of tumor position and subsurface anatomy. While this automated skin-fiducial localization method can be used in the context of many surgical domains for image-to-physical registration, in this work it will be evaluated in the context of breast conserving surgery (BCS) due to the deformable nature of breast tissue.

With regard to the clinical application, there has been recognition that BCS could benefit from the addition of

improved surgical guidance in the process of tumor resection [11, 12]. In recent years, breast conserving surgery reoperation rates have plateaued at approximately 10-20% [13]. Primary contributors to these reoperation rates are the vast shape changes and deformations between diagnostic and surgical settings that make it difficult to reliably determine intraoperative tumor positioning and extent [14-17]. To address these shortcomings, an automated surface acquisition method is needed to continuously inform an image-to-physical alignment approach that enables intraoperative visualization and localization of tumor boundaries established in preoperative MR imaging. More specifically, an image guidance system can use this stream of intraoperative surface points to continuously register a preoperative image to the patient in the operating room, and provide the surgeon with the location of their tools in relation to the tumor and other breast anatomy. Breast image guidance systems often rely on rigid registrations with less than 10 corresponding surface points [18, 19]. Extending beyond rigid alignment, a system that could measure 15-25 precise fiducials over the breast surface would potentially enable deformable soft tissue alignment techniques to facilitate lesion localization in the deforming breast during surgery. Since registration accuracy is ultimately dependent on data sparsity and coverage, the ability to quickly and accurately measure sufficient intraoperative localization data is critical for the utilization of image guidance. Corresponding points, i.e. points visible both in the preoperative image and on the breast in the OR, are an essential data source for guidance and correction frameworks. Though many approaches exist to measure 3D breast surfaces [20-24], to the best of our knowledge no approach exists to automatically extract landmark data from these breast surfaces in order to drive image-to-physical registration. Interestingly, even systems that acquire full surface data, rely solely on landmarks to provide alignment [18, 19], or incorporate landmarks to greatly reduce errors [23].

To visualize intraoperative tumor boundaries, several image guidance systems for breast conserving surgery have emerged using corresponding fiducial points [5, 6, 19, 25, 26]. These initial research systems for BCS used rigid registration to align preoperative supine MR images to the patient in the surgical position. For example, Barth *et al.* developed a guidance approach using skin fiducials and rigid registration to actively guide surgery. The image guidance system nearly halved positive margin rates of residual cancer after resection when compared to conventional wire guidance, from 23% to 12% [19]. Though this study showed great promise, the results were underpowered for statistical significance.

Another research prototype system for intraoperative breast tumor visualization used six ArUco tags to register virtual breast data to the patient and present the scene in mixed-reality [6]. These ArUco tag fiducials were not placed directly on the breast, but rather at the breast perimeter on the surrounding rib cage and just inferior to the clavicle, likely to avoid the dynamic deformations associated with soft breast tissue. While this placement provided rigid alignment, these fiducials could not capture the nonrigid shape changes [6]. Furthermore, the authors acknowledged difficulties in placing ArUco tags on

corresponding locations associated with MR-visible fiducial locations.

These rigid registration frameworks leave conspicuous residual misalignment after rigid registration [6]. To provide further context to the application, in BCS the patient's arms are outstretched at 90° (in a T-shape), whereas in a conventional closed-bore MR imaging system, the patient's arm would be positioned either down by the torso or up by the head to fit within the scanner. Though diagnostic MR imaging is generally performed in the prone position, tumors can change shape, volume and position when the patient moves to a supine position for surgery [14-16]. Many emerging guidance technologies rely on supine imaging [5, 18, 19, 26-32]. However, even when imaging and surgery are both performed with a supine body orientation, there are still large differences between imaging and surgical presentations that result in high residual alignment errors [33]. Quantitatively, for supine imaging-to-surgery position changes maximum target errors after rigid registration were reported from 10.7-36.4 mm, indicating that a rigid registration approach is unlikely to be sufficiently accurate for resection.

Beyond providing landmarks for rigid alignment as in the above systems, fiducials that are properly distributed across the breast could be used as a valuable source of deformation measurement [33] toward correcting misalignment due to breast shape changes [31, 34]. For example, Conley *et al.* presented a modeling framework with an initial rigid alignment using fiducials and ultrasound measurements of the chest wall followed by nonrigid correction driven by 6–7 surface fiducials [18]. While quite preliminary, compared to rigid registration the method improved tumor localization in surgical positioning by 15% and 58% in the two cases evaluated. A method presented by Ebrahimi *et al.* used thin plate splines to predict volumetric breast deformations from 24-34 surface fiducials alone. In six patients, the average estimate of a tumor centroid had 3-18 mm of error after rigid registration, and 1-10 mm of error after the thin plate spline registration scheme [31]. Expanding on the work of Conley *et al.*, a recent method for nonrigid correction driven with sparse ultrasound chest wall measurements and 23-26 fiducials reduced alignment errors by 50-60% over rigid registration when evaluated across surface fiducials and subsurface targets [35].

These advances toward sophisticated guidance approaches in BCS are encouraging, and common to the above systems is the need for intraoperative localization of fiducials, either by manual designation with an optically tracked stylus or by direct tracking with the use of an adhered marker. With the former, designating fiducial positions manually during surgery is tedious and the precision is heavily dependent on the user. Additionally, for soft tissues, measurement methods that contact the surface have been shown to be less accurate than noncontact measurements [36]. Despite the impracticality of manual methods, the latter option of adhered fiducials is complicated by the fact that fiducials near the surgical region of interest must be removed prior to commencing surgery. In [19], all fiducials are removed for surgery, limiting correction to only an initial alignment. Additionally, both methods are limited by
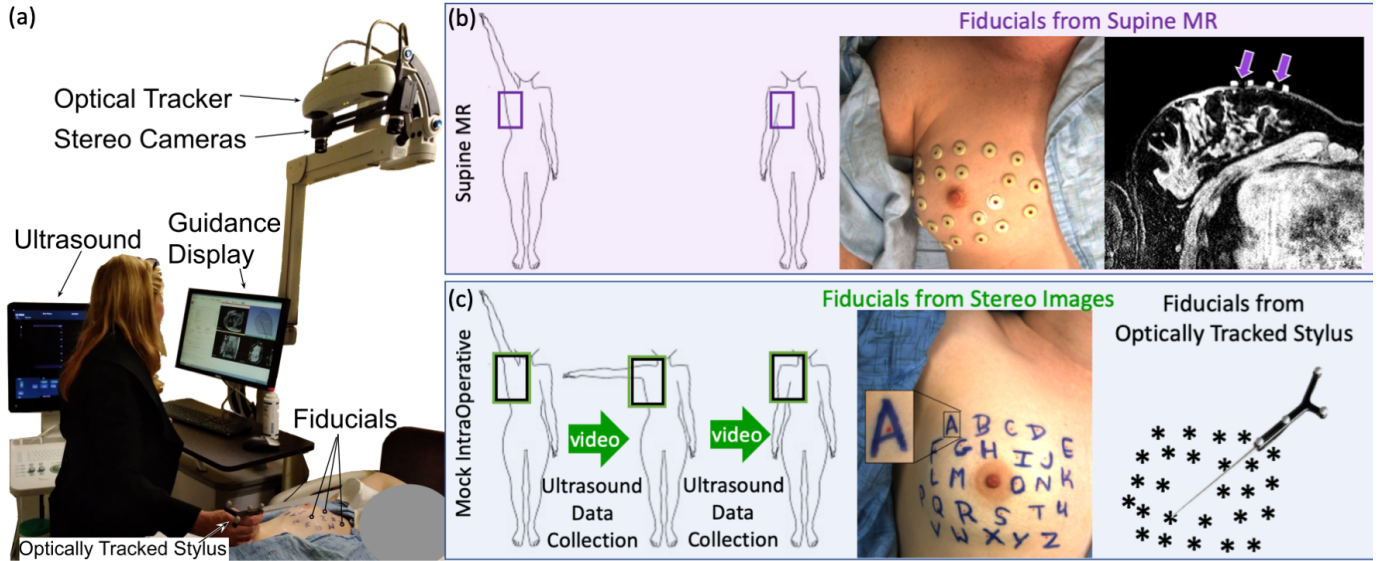
Fig. 1 Overview of data collection and the arm configurations, or states, measured in each setting. (a) image guidance system (b) data collected from supine magnetic resonance (MR) images (for error filtering) with the distribution of fiducials. In the top right, fiducial positions visible in an axial image slice are indicated with purple arrows. (c) data collected in the mock intraoperative setting.

non-automatic measurement and labeling of fiducials, which consumes valuable time in the operating room for each additional fiducial identified during the procedure.

The landscape of emerging guidance systems for BCS reveals a pressing need for rapid soft-tissue measurement techniques that can easily integrate into BCS workflow to enable novel alignment and localization approaches. The work presented here directly addresses this need by abandoning the concept of structured or printed fiducials, and instead investigating a novel approach with intuitive (English alphabet) fiducials inked directly on the breast surface and then tracked using image processing methods. The strategy is easily integrated into current workflow and the inked letter-based fiducials on the patient inherently correspond to labels that can be rendered in an image-guided display to provide surgeons with a convenient, intuitive map on a previously featureless breast surface. The automatic surface acquisition method uses simple image processing to detect fiducial labels and fiducial positions, and leverages conventional feature detection and matching to track these fiducial positions on the nonrigidly deforming skin surface through time. These fiducials that consist only of sterile ink can be tracked to provide continuous, automated, simultaneous, and precise fiducial collection in a dynamic operating room setting.

II. METHODS

A. System Overview

As noted above, the BCS guidance instrumentation landscape is rapidly evolving and the realization under investigation here is shown in Figure 1a. For the sake of clarity, the overarching system is discussed here as an example use case. Briefly, the MR-visible fiducials shown in Figure 1b are adhered to the breast with images acquired in the supine breast orientation to closely resemble surgical positioning (note that abducted arm is not typically possible in conventional closed

bore MR systems). After imaging, these fiducials can be ink-marked directly on the skin, and then removed to provide a set of corresponding fiducials visible in both preoperative MR imaging and intraoperative physical space. The computer vision instrumentation of Figure 1a and the methods described below are used to track fiducial deformations continuously during surgery. The mock surgery challenge is shown in Figure 1c with independent stylus measurements available for validation (Figure 1c-right). With respect to the goals of the investigation herein, the methods, robustness, and accuracy associated with the intraoperative tracking phase (Figure 1c) are reported. However, it is important to note that the MR-fiducial position configuration acquired in Figure 1b serves as an initial spatial prior to enable error filtering for the intraoperative tracking methods described below. While the intraoperative measurement phase is the focus below, the MR imaging data components are included for completeness. Lastly, the process of utilizing these types of intraoperative deformation measurements to nonrigidly align the 3D supine breast MR-imaging volume to the physical tissue field has been addressed in a previous work [35].

B. Human Data Collection

Using the system shown in Figure 1a, data were collected on *n=8* breasts across six healthy volunteers ages 23–57 (29 ± 14) with informed consent and approval from the Vanderbilt University Institutional Review Board (protocol code 130038, date of approval 11/11/2015). For two subjects, data were collected on both left and right breasts. For each breast, 26 MR-visible fiducials (IZI Medical Products, Owing Mills, MD) were distributed on the breast surface. Supine MR images were obtained in two arm positions shown in Figure 1b: with the ipsilateral arm down resting beside the torso, and with the ipsilateral arm up resting beside the head. The arm-up MR image is considered the preoperative image for the arm-up mock-OR configuration, while the arm-down MR image is used

as a prior for the mock intraoperative states with the arm fully adducted, and in surgical position. Fiducial positions were manually designated in each MR image. At least 24 fiducials were visible in each MR image, with some fiducials going out of view due to image size and large deformations from arm abduction. On average, 25.6 ± 0.6 fiducials (mean $\pm$ std) were designated within an individual MR image volume.

After imaging, subjects were moved to a mock intraoperative setup where they lay supine with padding under the ipsilateral shoulder to simulate rotation of the OR table. The center of each toroidal MR-visible fiducial was marked with colored ink (red) shown in the center image of Figure 1b, and the fiducial was removed. Each fiducial, now a red dot, was then labeled with a capitalized English character in a second color ink (blue letter label) as in the center image of Figure 1c. The size of each character was approximately 3 cm in height, and each fiducial dot was approximately 2 mm in diameter. Visible skin markings (such as moles) that were the same color as fiducials were covered with a third ink color. Static fiducial locations were measured in three positions for each breast: arm up, surgical position (i.e. arm outstretched at 90°), and arm down. Fiducial locations were also designated manually using an optically tracked stylus (Polaris Vicra optical tracker, Northern Digital, Waterloo, ON, Canada), a tool typical in image guided surgery.

Stereo images of the mock-operative field were collected with two Grasshopper stereo cameras (FLIR, formerly Point Grey Research, Richmond, BC, Canada) placed 0.9-1.2 m above the skin surface. Stereo cameras provided color images at 1200x1600 pixel resolution, and were calibrated using the method presented by Zhang *et al.* [37] in MATLAB's Computer Vision Toolbox [38]. This calibration defines the relationship between the two stereo cameras. The point's depth is constrained by its positions in the 2D images, and the known relationship between the cameras. Therefore, the 3D position can be triangulated, or reconstructed, from localized and matched 2D point locations. Reprojection error after calibration was on the order of 0.2-0.4 pixels. Stereo cameras were used to record videos of fiducial positions in the three static arm positions and throughout arm adduction at about 5 frames per second. Intermittently during video collection, an ultrasound exam was conducted, providing procedural obstruction of the visual field. Video footage recorded during this process consisted of ultrasound gel application, probing the ultrasound transducer over the breast surface, and gel removal with a towel. Video frames were considered static if they contained breathing motion, but no other major motions, obstructions, or interference with breast tissue. Thin layers of ultrasound gel were not considered an obstruction. To assess realistic tracking performance, the algorithm tracks fiducial points throughout the full video duration, including arm adduction and ultrasound exams. This allows analysis before and after considerable motion and obstruction events.

C. Algorithm Overview

This surface tracking algorithm for image guided surgery uses handwritten inked fiducials that can be sterilized and remain on the skin throughout surgery. The algorithm is implemented in MATLAB 2021b using functions from the Computer Vision Toolbox [38]. Briefly, fiducials are localized in 2D images by leveraging the two ink colors and adaptive thresholding [39]. Fiducials are matched and tracked using KAZE feature matching [40] and point history. An overview of the algorithm is shown in Figure 2, best viewed in color. The algorithm is considered in two parts: localization and labeling.
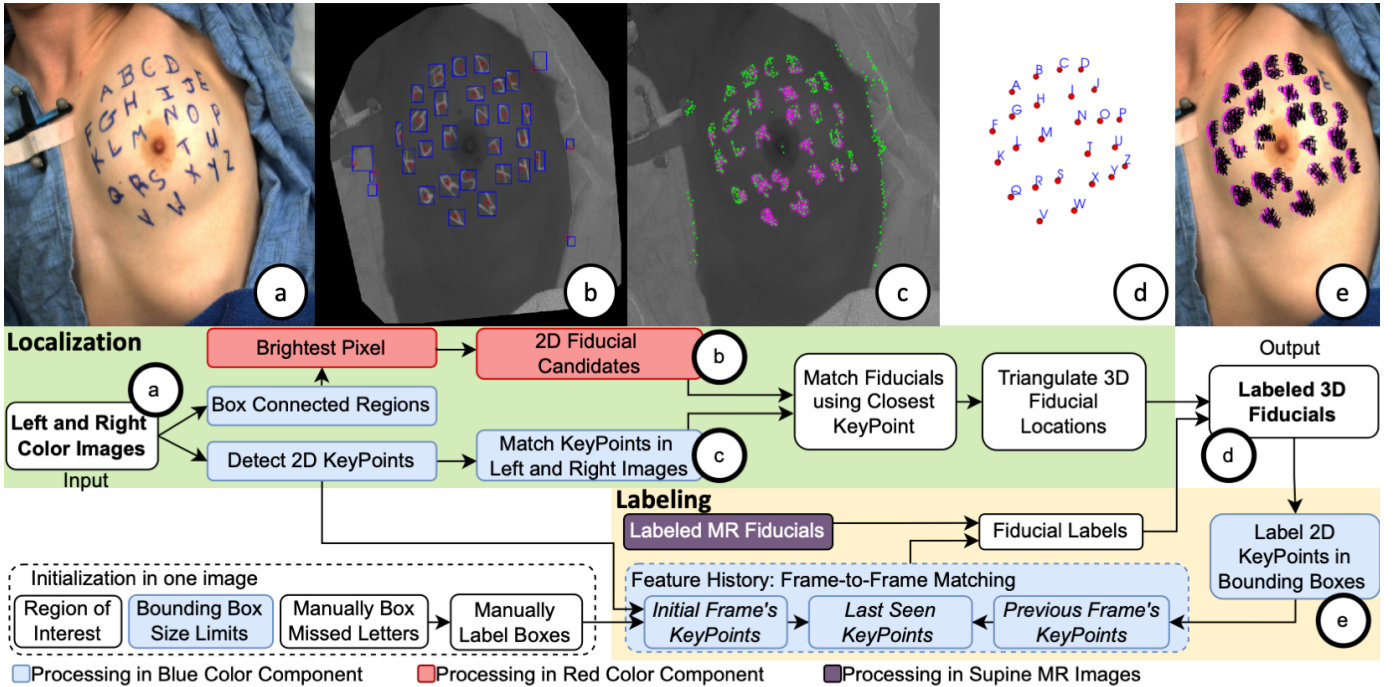

Fig. 2 Detection and tracking algorithm. Images cropped for visualization. (a) A color image from one of the stereo cameras (b) blue color component of the masked region of interest with boxed connected regions (blue), and 2D fiducial candidates (red) (c) 2D KAZE keypoints (green) with successfully matched 3D keypoints circled (magenta) (d) Output labeled fiducials in 3D space and (e) 2D keypoints labeled by bounding box for input into the feature history.

D. Fiducial Detection: Point Localization

The color component is computed from the raw RGB camera images as the color ratio of each pixel according to

$$Color\ Component(c \in \{R, G, B\}) = \frac{c}{R+G+B} \qquad (1)$$

for R, G, and B the red, green, and blue intensities, respectively, where c is the desired color channel. The color component range is normalized to 256. In the blue color component ($c=B$), adaptive thresholding is used to create a binary mask of the letter label regions. A bounding box is placed around each connected component. Within each bounding box, the red color component image ($c=R$) is computed and individually normalized to 256. This process provides maximum contrast between fiducial pixels and surrounding skin, from which a 2D fiducial candidate is identified as the centroid point in the region grown around the brightest pixel in the red color component. In Figure 2b, the blue color component image shows the bounding boxes resulting from adaptive thresholding in blue and the identified 2D fiducial candidates circled in red.

KAZE feature detection and matching is used to obtain a sparse cloud of triangulated keypoints [40]. Detected KAZE keypoints (2D keypoints) are shown in Figure 2c in green, with keypoints successfully matched between left and right stereo images (3D keypoints) plotted as magenta circles. The 2D fiducial candidates from the red centroids are matched as follows. For each 2D fiducial candidate in the left image (candidate$_L$), the algorithm determines the closest successfully matched keypoint from KAZE (keypoint$_L$, where its successful match is keypoint$_R$). In the right image, the 2D fiducial candidate (candidate$_R$) closest to the keypoint$_R$ is considered the correct match. Although KAZE produces a 3D point cloud (visualized in 2D space as the magenta circles in Fig. 1c), the keypoints have no correspondence to the MR image. This process of fiducial detection and matching ensures measurements of the inked fiducial points that correspond to imaging data. However, it should be noted that the closest-keypoint assumption does yield some incorrect matches. Outliers are removed at this step by error filtering based on the difference in pixel-wise positions between left and right matched points. Outliers are filtered first by Δy (where $\Delta y \approx 0$ for these rectified images), then by Δx (to remove outliers that represent unrealistic depth values). Next, matches are ensured to be unique. For all nonunique matches between fiducial candidates, the best candidate is chosen by the match that provides a difference vector $[\Delta x, \Delta y]$ closest to the median difference vector of all matched keypoints.

E. Initialization

On initialization, the user manually defines a single region of interest (ROI) for each camera and tunes the minimum and maximum letter bounding box sizes according to the size and variability of the letter labels. The main purpose of the ROI is to reduce the computational search space for several of the tracking steps. This reduction improves runtime for feature detection and eliminates many extraneous 2D fiducial candidates in an early phase of the algorithm. After the ROI is established, the ROI is dilated before applying the adaptive thresholding step on subsequent frames to ensure that the mask edge is sufficiently far from the letter labels and does not interfere with thresholding. Returned fiducials are required to be within the true, undilated ROI. Bounding box size limits are manually set to include all letter-labels. These four values (x_{min}, x_{max}, y_{min}, y_{max}) are defined once and applied to both image streams.

Once the detection algorithm is initialized, the tracking algorithm is initialized in just one image. After automatic 3D fiducial detection, the 2D bounding boxes of these 3D candidates are presented to the user. For the case shown in Figure 2, there are 25 boxes presented to the user: boxes around all letters except "E". The boxes are a subset of the blue bounding boxes displayed in Figure 2b. The user is instructed to manually box undetected fiducial labels (e.g. "E" in Figure 2b), and manually label each box with its letter label. This user input serves to initialize the feature history. All 2D keypoints that fall within labeled bounding boxes are stored along with their features and labels. Examples of these labeled keypoints are shown in Figure 2e.

Finally, when fiducial candidates arise too close together, e.g. due to a letter-label appearing discontinuous in an image, the candidate with the highest red color component intensity (averaged candidate intensity in the left and right images) is kept and all other candidates are discarded. The algorithm therefore requires one additional parameter that defines a minimum allowable distance between fiducial candidates in 3D space. For the majority of cases, this parameter can be zero (unconstrained). However, for one case (case 1L), the parameter was set so that 3D fiducial candidates must be at least 20 mm apart.

In summary, initialization includes manually annotating in the first image frame: (1) one ROI for each camera, (2) bounding box size limits, (3) bounding boxes missed by automatic detection, (4) letter labels for bounding boxes, and (5) minimum distance between fiducials.

F. Fiducial Tracking: Point Labeling

In order for intraoperative camera data to be registered to a preoperative image, the fiducials must be labeled, defining correspondence to the fiducial positions in the MR image. Automatically labeling the 3D fiducial candidates relies on frame-to-frame KAZE feature matching [40]. In summary, labels are propagated through one camera stream by matching the 2D keypoints within bounding boxes to previously labeled keypoints. The label of a fiducial candidate is the most common label in its bounding box.

Feature matching relies on storing feature history in three main phases: *Phase 1*: keypoints in the initial frame, *Phase 2*: keypoints in the previous frame, and *Phase 3*: the last seen keypoints. The feature history stores keypoint locations, feature vectors, and letter-labels. In *Phase 1*, a new frame's intra-bounding-box keypoints are matched to keypoints in the initial frame; the initial frame's feature labels have the highest confidence since they were manually specified at the start of the procedure as described in the previous section. In the new frame, only unlabeled bounding boxes continue on to be labeled by the next phase. Next, in *Phase 2*, keypoints in these remaining bounding boxes are matched to the keypoints of the

previous frame. The previous frame is most likely to resemble the current presentation of features. Finally, the remaining unlabeled bounding boxes continue on to *Phase 3* where keypoints are labeled using the last seen keypoints. The list of last seen keypoints for a given letter is defined as the most recent 100 points labeled with that letter. Since there are 26 fiducial letter-labels, the size of this matrix is therefore restricted to 2600 features, letters, and point locations (recall that the feature history is only maintained for one camera image stream). When constructing the last seen keypoint matrix, points are added in descending time order prioritizing points that were successfully matched to the current frame. In priority order, points are added from the following lists until 100 features are reached: (i) matched features from the previous frame, (ii) matched features from the last seen keypoints, (iii) unmatched features from the previous frame, and (iv) unmatched features from the last seen matrix. The last seen points add robustness to lighting variations and occlusions.

After all boxes are labeled, uniqueness is enforced again. Letter duplicates are evaluated and the 3D fiducial candidate closest to the historic 3D fiducial location is kept, while all other candidates labeled with that letter are discarded. If the letter has not been previously localized in 3D, the point location is considered uncertain and all candidates for this letter are discarded.

Here, a final stage of error catching is implemented that is unique to this application. Points that are sufficiently far from their MR counterpart are considered erroneous. More specifically, image-to-surgery rigid registration accuracy in the supine position has been previously measured with maximum surface target errors between 7.4 and 36.4 mm [33]. Using this characterization as a guide, fiducials were considered incorrectly localized if they were more than 40 mm from their MR fiducial counterpart. While this parameter is a constant in this work, if 40 mm proved inappropriate on another dataset, this parameter could be prescribed based on fiducial registration error (FRE) after the point-based registration of the tracked fiducials to their positions in preoperative MR. This error catching largely serves to remove points with incorrect left-right matching causing erroneous triangulated 3D coordinates.

G. Evaluation

Three main performance metrics are evaluated: (A) localization accuracy of 3D fiducial detection, (B) tracking fidelity, and (C) tracking completeness.

Beginning with the detection algorithm localization accuracy, 3D localized fiducial points were compared to the corresponding points localized using an optically tracked stylus tool (NDI Polaris Vicra, Waterloo, Ontario, Canada), which is a standard in image guided surgery due to its reliable accuracy [41]. In each static arm position, the fiducial positions as measured with the stereo cameras are automatically localized and manually labeled. Note that the detection and localization steps do not provide labels. Though labels are usually provided by tracking, here the evaluation focuses on localization accuracy while removing tracking accuracy as a confounding factor. The camera-based fiducial measurements are rigidly registered to positions measured with the optically tracked stylus and the residual error is reported. Registrations are

computed using a conventional least-squares singular value decomposition point-based registration method [42], and fiducial registration error (FRE) is measured as the root mean square of the distances between registered point sets as defined by Fitzpatrick *et al.* [43]. Additionally, to measure the accuracy of the gold standard measurements, for one subject, fiducial positions were measured repeatedly with the optically tracked stylus. All combinations of these point sets were rigidly registered, and the average FRE is reported as a baseline error metric for this ground truth measurement technique.

With respect to assessing tracking fidelity, the rate of false positives, i.e. incorrect fiducials returned, was measured by examining fiducial positions in the 2D images, and by comparing 3D triangulated fiducial locations to stylus-designated locations. The number of frames with no false positives is reported and represents how often the automatically detected fiducials can be used for reliable image-to-physical registration. For a frame f, the false discovery rate (1-precision) is described as

$$False\ Discovery\ Rate_f = \frac{False\ Positives}{Total\ Detections} \times 100\ \%. \quad (2)$$

The average false discovery rate is reported.

Lastly, tracking completeness is evaluated with the number and distribution of visible fiducials not returned as output. In other words, this section analyzes how many fiducials are missed, and how these missed fiducials are distributed across the breast surface. To compare the automatic method to an ideal output from the stereo camera images, detection rate (recall) is considered as

$$Detection\ Rate_f = \frac{True\ Positives}{Total\ Visible} \times 100\ \% \quad (3)$$

where the total number of visible fiducials is determined as the number of fiducials that could be localized in the camera images by augmenting automatic detection with manual point picking. Fiducials are considered not visible if their red fiducial centroid cannot be picked manually in the stereo camera images for a state. The analysis is extended to investigate completeness with regards to the full extent that could be captured with an alternative method not limited by line-of-sight (e.g. manually designated with tracked stylus) with

$$Extent_f = \frac{True\ Positives}{26\ fiducials} \times 100\ \% . \quad (4)$$

It should be noted that the number of frames in each breast acquisition state analyzed is not necessarily evenly distributed as no specific protocol was in place for the length of time recorded in each static arm position. Since arm up configurations generally expose a greater number of fiducials to the cameras, an unweighted average may show that cases with more frames in the arm up position have better completeness metrics. To remove this bias, completeness metrics for each case are first averaged by state, then averaged across all three states. Additionally, the completeness metrics did not include phases of motion or obstruction.

III. RESULTS

A. Detection: 3D Localization Accuracy

Localization accuracy was evaluated in the three static arm states (one evaluation per state) for seven of the eight cases. One case, case 5R, was omitted due to missing still images time-synced with NDI collection. Accuracy is reported as the FRE
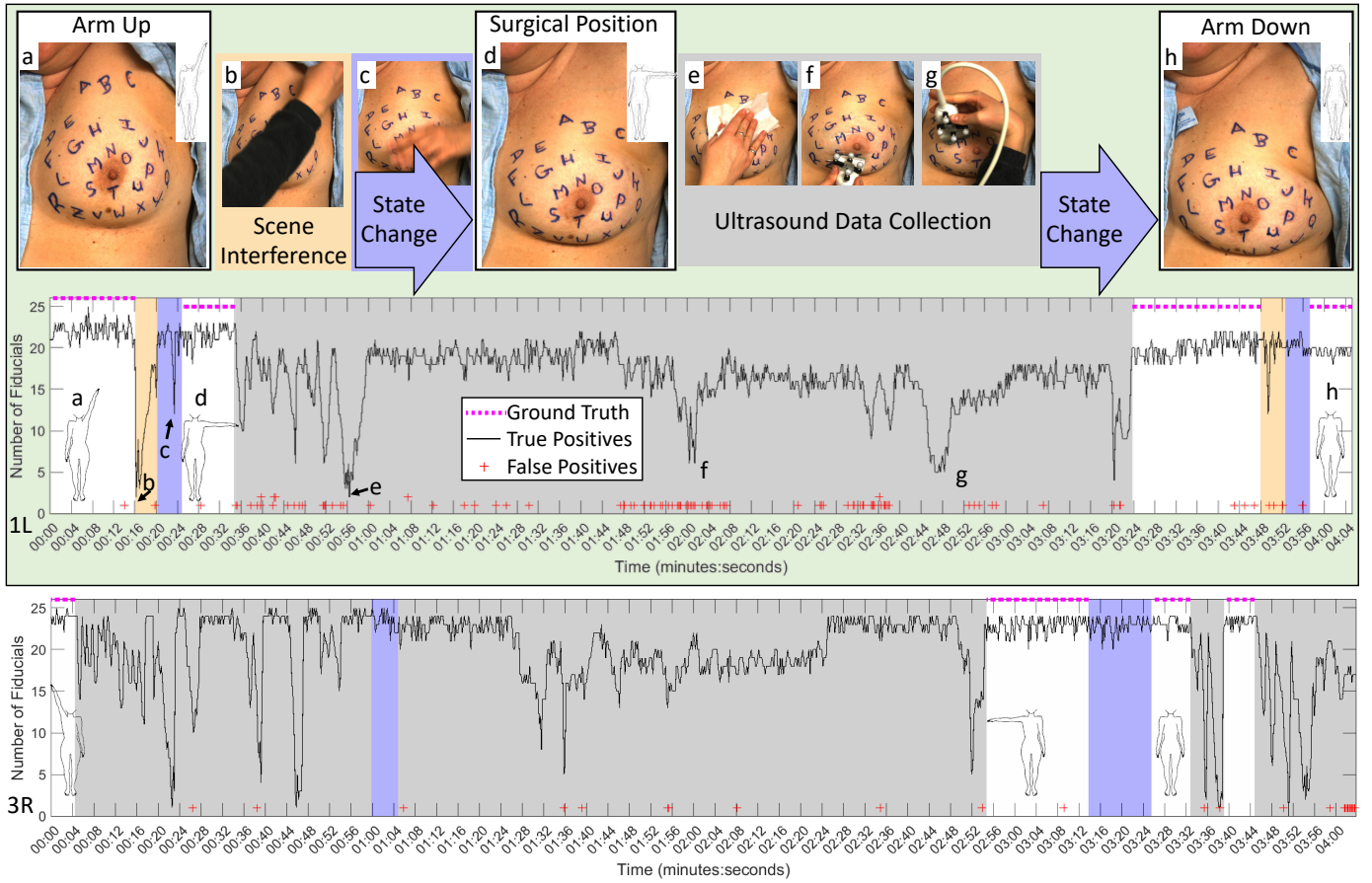
Fig. 3 Data collection and processing throughout the entire video for two representative cases: 1L and 3R. Note performance recovery after obstructions and false positives. The three arm configurations where accuracy was measured are overlaid: arm up (left), surgical position, and arm down (right). Video content is classified into four categories: static frames (no highlight), adduction frames (blue), ultrasound collection (gray), and other scene interference (yellow). Number of fiducials that are true positives (black line), false positives (red +), and manually localized in static frames (magenta dashed line). Highlighted frames are processed but excluded from reported metrics.

associated with registering fiducial points localized from the stereo camera system and the corresponding points designated with an optically tracked stylus. On average, 22.0 ± 2.4 fiducials were automatically localized with the camera system. Table I reports the accuracy (FRE) and the average number of fiducials used to compute the rigid registration, averaged across all 3 states. After rigid registration, automatically localized fiducials differed from the ground truth stylus-designated positions by 1.6 ± 0.5 mm. As reported in [33], when static fiducial positions on the breast were measured with the optically tracked stylus repeatedly five times FRE was 1.5 ± 0.1 mm. The two distributions of FRE were compared with an unpaired t-test (α=0.05) and were not significantly different (*p*=0.54).

TABLE I
LOCALIZATION ACCURACY

CASE	AVERAGE ACCURACY (MM)	AVERAGE NUMBER OF FIDUCIALS LOCALIZED
1L	2.6	20.0
2R	1.9	25.0
2L	1.5	22.7
3R	1.6	23.7
4R	1.2	21.3
5L	1.4	23.0
6L	1.3	18.0
AVERAGE	1.6 ± 0.5	22.0 ± 2.4

B. Tracking: Fidelity

Tracking fidelity is only evaluated in static frames as these are the only acquisition times where the corresponding ground truth 3D fiducial locations (stylus-designated) are available for verification. Though a tracking algorithm should successfully track through large deformations and obstructions, it is reasonable to assume that surface data will be collected during static, unobstructed scenes. Here, all video frames were processed for tracking, though performance during deformations and obstructions is only shown for cases 1L and 3R. Figure 3 shows the true positive and false positives over time through the entire protocol for cases 1L and 3R. For these cases, full videos are available in the supplementary material with annotated algorithm performance. In Figure 3, the video frames from various experimental phases are displayed for case 1L, demonstrating how obstructions in the scene result in a lower number of localized fiducials. The total number of frames processed for tracking and the number of static frames analyzed are reported in Table II alongside the false discovery rate and the total number of false positives. Since no frames had more than one false positive, the number of false positives also represents the number of frames with unusable output for registration. In the worst case (5R) where 7/267 frames have false positives, still over 97% of frames are usable for reliable

registration. Overall, on average 99.1 ± 1.1 % of frames are usable.

TABLE II
TRACKING FIDELITY

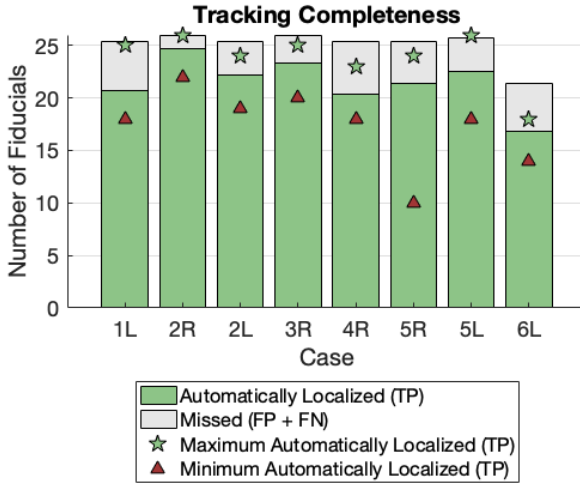| CASE	TOTAL FRAMES TRACKED	STATIC FRAMES ANALYZED	TOTAL FALSE POSITIVES	FALSE DISCOVERY RATE (%)
1L*	1227	295	5	0.1
2R	1507	431	0	0.0
2L	874	206	0	0.0
3R*	1220	185	1	0.0
4R	582	132	3	0.1
5R	1312	267	7	0.2
5L	790	129	0	0.0
6L	575	171	0	0.0
AVERAGE	1011	218	2	0.1 ± 0.1

performance visualized in Figure 3

Fig. 4 Average number of fiducials automatically localized (TP= true positives), compared to the average number of fiducials visible (top line of each bar). False negatives (FN) and false positives (FP) are considered missed fiducials.

C. Tracking: Completeness

The average detection rate was 85.6 ± 5.9%, showing that a large majority of visible fiducials can be automatically detected and localized as visible in Figure 4. All static frames returned at least 10 fiducials for registration, with 75% of cases returning a minimum of 18 fiducials across all frames. In retrospective analysis, the fiducials that were more frequently missed resided on the lateral edge of the breast surface, closest to the arm, where the surface deviates from relative planarity as displayed in Figure 5. While highly performant, the algorithm was found to struggle with some letter distortions due to large deformations. To illustrate this trend, the magnitude of deformation due to arm adduction is shown in the right column of Figure 5. This drop-out due to distortion is most notable in the upper outer breast quadrant (i.e. fiducials closest to the armpit) like the letter "C" in the top row of Figure 5. Also, it is interesting that not all fiducials with large displacements suffer: more medial fiducials that undergo large deformations are able to be localized with low dropout rates (e.g. the letter "B" in the top row). With regards to extent, although the cameras suffer from line of sight constraints, 82.6 ± 9.2% of the full 26 fiducials can be localized automatically (Figure 5 – *Center* column).

IV. DISCUSSION

This work demonstrates a successful surgical field monitoring system that can capture nonrigid skin motion with accuracy, fidelity and completeness such that it can be used to promote new directions in surgical guidance. The inked fiducials are easy to place and are amenable to sterile processes, as they can remain on the skin surface throughout surgery. The large letter label provides a feature rich surface and the small fiducial dot provides a precise localization target. These labeled landmarks localized both on the breast skin and in preoperative imaging can be used to drive a registration framework for visualizing and navigating around tumor boundaries and other breast anatomy. While quite preliminary, initial surgeon impressions with the lettered fiducials integrated into a guidance system were met with considerable enthusiasm as letters provide naturally understandable landmarks between the patient and the guidance display.

In comparison to existing alternatives that for BCS intraoperative fiducial measurements, localization accuracy for automatic detection was not statistically different from manual digitization using an optically tracked stylus. However, it should be noted that the accuracy of stylus-designated data is
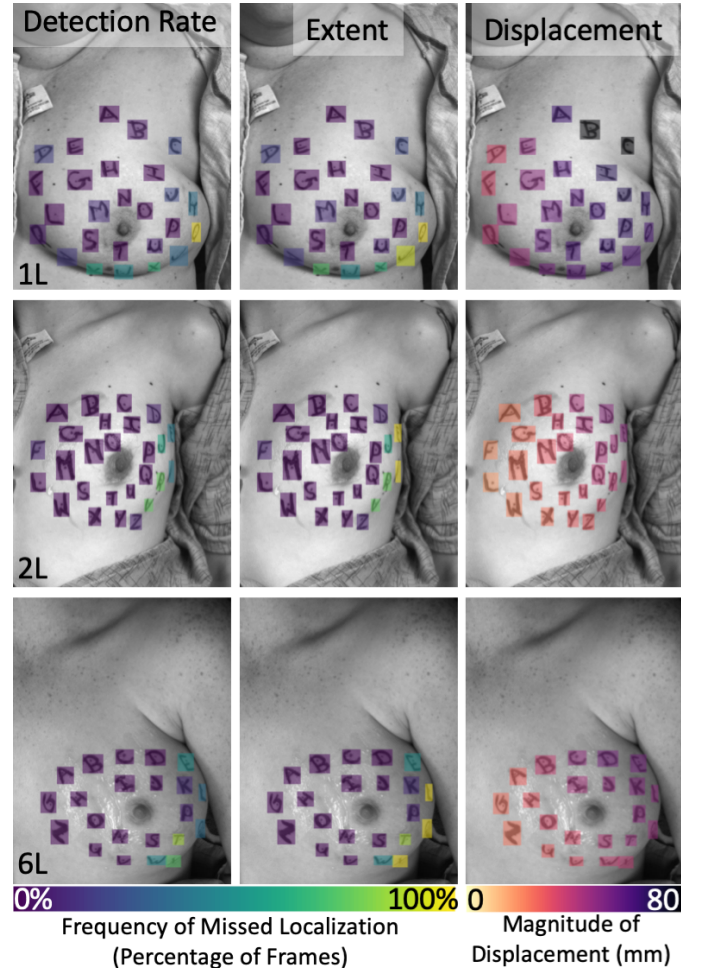

Fig. 5 Distribution of missed fiducials for three cases, shown in the arm-down state. *Left* - detection rate, or missed fiducials with respect to all visible fiducials. *Center* - extent, or missed fiducials with respect to all 26 placed fiducials. *Right* - fiducial displacement from arm up to arm down states.

user-dependent which was noted during data collection. For example, manual stylus digitization without deforming the surface was challenging while the subject was breathing.

Though this work focuses on the algorithm's utility within image-guided breast surgery, the advancements presented here are relevant to other organ systems and applications as well. While this method would be more difficult to apply to an internal organ system, it could have applications in other surface organs, such as the abdomen, for image-to-physical registrations for guiding percutaneous abdominal interventions [4] or for patient positioning in radiation oncology [44].

As a general note, the tracking algorithm presented here was designed and evaluated within the context of utility in image guided surgery. While some algorithms may balance all evaluation metrics, utility in the surgical guidance application relies on a low false positive rate, as frames with false positives cannot be used for registration. Consequently, aggressive error catching was implemented to prioritize a low false positive rate over a high detection rate (i.e. it is preferable to miss some fiducials, as long as all fiducials are trustworthy).

The tracking algorithm is highly reliable with a low false positive rate suitable for use in surgery. The algorithm suffers most with completeness, as line-of-sight constraints can confound detection rate and extent. For example, for the two subjects that had both breasts processed, the breast with better line-of-sight (i.e. larger simulated rotation of the table to provide a more favorable viewing angle) performed better. For case 2, the right breast was more favorably angled than the left, and for case 5 the left breast was more favorably angled than the right. Intra-subject performance differences are visible in cases 2 and 5 in Figure 4, with 2R and 5L outperforming their counterparts.

Despite line-of-sight constraints, an adequate number of fiducials can be localized for a reliable registration. The minimum number of localized fiducials for most cases was above 15, far more than the 6-8 fiducials used for registration in initial breast guidance methods [18, 19], or the 11 fiducials necessary to fully describe rigid breast deformations [33]. On average, 21 fiducials could be localized, providing distributed coverage of surface data to drive potential nonrigid correction frameworks.

For case 5R, there were two frames where only 10 fiducials could be automatically localized. This low minimum was due to a reduced point cloud returned from KAZE feature matching whereby fiducials were still correctly detected in each image, but the algorithm failed to successfully match keypoints between left and right images. This case suffered from a variety of confounding factors: white-balance discrepancies between left and right images, shadows, and subtle motion due to subject re-adjustment. Though all of these problems are visible in other cases, we hypothesize that the combination of all three factors caused the unusual dip in the number of localized fiducials.

As noted in Section III.C, largely distorted fiducial labels become more difficult to match to the object's feature history. This effect may be particularly detrimental as points with large displacements are likely to be the most informative to registration. However, the breast would not be subjected to the full range of arm motion intraoperatively–only half the range of motion is needed to move from imaging position (arm up or down to fit within a closed bore scanner) to intraoperative position (90° abduction).

With respect to limitations, there are several aspects that are important to consider: (1) skin tone variations, (2) ink colors, (3) lighting variations, (4) processing time, and (5) reproducibility.

Beginning with skin tone variations, these were not explored in this manuscript as all volunteers for this study were Caucasian. Evaluation on a variety of human skin colors remains to be evaluated. However, the algorithm is specifically designed with skin tone variations in mind, with fiducial detection performing well in the blue color component images across phantoms of various skin tones [45] from previous work. A predecessor to the detection process presented here is described in [45] though correspondence between 2D fiducial candidates was determined with optical character recognition. The previous approach showed that this 2D detection method was robust to phantoms of differing skin tones; however, the algorithm experienced large dropouts at the correspondence step due to the poor performance of the preliminary optical character recognition approach.

When reflecting on the second limitation of ink colors, it is important to consider the use of red ink in light of the eventual presence of blood after incision. In this work, an algorithm that leveraged two ink colors on opposite sides of the color wheel was implemented. Though the concept of color channels is leveraged heavily in this approach, the color channels do not need to be prescribed to blue and red. Preliminary investigations not reported here show that alternative ink colors can be transformed in hue saturation value (HSV) space to map the label color to an equivalent of the blue color channel, while mapping the fiducial color to the red color channel. The use of purple letters and green fiducial centroids is under consideration currently. More comprehensive evaluation of algorithm performance under these conditions remains to be investigated further. In regards to scene interference in the pertinent color channels, the algorithm may struggle with potential skin discolorations (e.g. bruising). Though a third color ink could be used to cover skin markings, ink-covering of these regions may not always be possible. It should be noted that here the ultrasound gel was tinted blue (the same color as letter-labels), and in some cases residual gel remained spread across the breast during the static frames evaluated. While the algorithm sometimes struggled with specular reflections from ultrasound gel, the color tint generally did not interfere with adaptive thresholding. Scene interference in the red color channel (e.g. the red cap of the ultrasound gel bottle) is generally more intrusive to performance, as obstructions close to the true fiducial location can cause false positives. This can be observed in the supplementary videos.

With respect to lighting variations, while some insight was gained from the introduction of ultrasound gel, more investigation is needed. Apart from glare on the gel, the videos acquired did include footage containing moving shadows, but it is difficult to study the impact given that the bright overhead

lights typically present in the OR were not part of our mock surgery experimental setting. With proper exposure, the breast surface should be clearly illuminated with little impact on algorithm performance although future investigations are warranted.

Runtime evaluation, the fourth limitation, also remains to be optimized. The current processing rate is about 2.5 seconds per frame, with the large majority of that time spent on KAZE feature detection and matching. Speed improvements could be achieved by implementing this algorithm on a graphical processing unit (GPU) in an a more efficient programming language than MATLAB and by using AKAZE feature matching. Accelerated KAZE has shown dramatically improved speeds with little effect on matching performance [46], and KAZE implementations on a GPU have been shown to offer tenfold speed improvements with no degradation in performance [47]. Machine learning approaches may also offer speed improvements; however, they may be particularly limited by a small mock-intraoperative dataset. The system presented in this work could be deployed in surgery and used for guidance while simultaneously collecting a representative dataset for future investigations into machine learning approaches. Future machine learning approaches should also be careful to remain unbiased to skin tone variations. Additionally, improvements to various aspects of the algorithm may introduce new pitfalls. For example, a more complete keypoint cloud could yield better tracking on steeply curved surfaces, but would likely require more error filtering due to difficulties localizing fiducials on the breast edges (e.g. due to shadows or line-of-sight constraints). Nevertheless, the current implementation can provide continuous updates with a sampling rate of 2.5 seconds. Similarly, it can provide on-demand updates to a guidance framework with minimal wait times. Although surgery would be briefly paused for a registration update, an on-demand framework would be far less intrusive than current clinical seed-based guidance approaches that require the surgeon to halt surgery and use a handheld probe to survey the field manually. Additionally, existing seed-based systems only provide a distance readout to a preoperatively implanted point-based target, which would be considerably inferior to accurately co-registered supine MR imaging data.

Lastly, when considering reproducibility, the algorithm assumes several constraints to data collection. As previously mentioned, each fiducial label should be continuous to provide an adequate bounding box. Labels should also be placed around the planned incision so that they are not split during resection. Though if a label is split, manual intervention with ink or re-initialization would allow continued tracking. Labels should ideally be unique, to ensure that features are correctly matched. For best performance, fiducial labels should be uniform in size which allows more erroneous boxes and fiducial candidates to be eliminated based on size limits. Some cases here have relatively nonuniform letter size and thickness (as visible in Figure 5), and it should be noted that thicker inked lines provide better performance in the adaptive thresholding stage, as thin lines may break into multiple boxes creating erroneous 2D candidates. While the algorithm was generally robust to these variations, standardizing fiducial size and line thickness may reduce erroneous candidates and improve performance further. In summary, inked fiducial type, coloring, and arrangement can influence performance and protocol to control these factors remains to be further investigated.

Despite these limitations, this methodology is evaluated on a challenging dataset that incorporates many realistic confounding factors from major and minor deformations, obstructions, and scene interference. The approach demonstrated accuracy and robustness (Tables I and II) that make it a promising solution for soft tissue monitoring in the OR.

V. CONCLUSION

This work presents a novel method for precise intraoperative fiducial localization that is robust to interference from tools, occlusions, and most distortions of the skin surface. Fiducial inked-letter labels provide an intuitive mapping between landmarks written on the breast and landmarks on an image-guided display to more easily orient the surgeon during surgical navigation. This approach is contactless, automatic, and localizes all fiducials simultaneously providing one snapshot of the breathing cycle. The surface acquisition process is amenable to surgical workflows with fiducials that can be hand-drawn, sterilized, and remain on the breast surface throughout surgery. This method opens opportunities to move breast guidance beyond initial single-shot rigid alignments and towards continuous correction allowing for automatic updates to an image guidance system. Going even further, by providing dense fiducial coverage with high fidelity and precision, this data can serve as input into a deformable correction method to improve the accuracy of breast tumor localization. The work presented here demonstrates clinical utility of computer vision for monitoring soft tissue in the surgical field.

REFERENCES

[1] F. Chadebecq, F. Vasconcelos, E. Mazomenos, and D. Stoyanov, "Computer vision in the surgical operating room," *Visceral Medicine,* vol. 36, no. 6, pp. 456-462, 2020.

[2] V. Mondéjar-Guerra, S. Garrido-Jurado, R. Muñoz-Salinas, M. J. Marín-Jiménez, and R. Medina-Carnicer, "Robust identification of fiducial markers in challenging conditions," *Expert Systems with Applications,* vol. 93, pp. 336-345, 2018.

[3] M. Fiala, "ARTag, a fiducial marker system using digital techniques," in *2005 IEEE Computer Society Conference on Computer Vision and Pattern Recognition (CVPR'05)*, 2005, vol. 2, pp. 590-596: IEEE.

[4] M. Solbiati *et al.*, "Augmented reality for interventional oncology: proof-of-concept study of a novel high-end guidance system platform," *European radiology experimental,* vol. 2, no. 1, pp. 1-9, 2018.

[5] P. F. Gouveia *et al.*, "Breast cancer surgery with augmented reality," *The Breast,* vol. 56, pp. 14-17, 2021.

[6] S. L. Perkins, M. A. Lin, S. Srinivasan, A. J. Wheeler, B. A. Hargreaves, and B. L. Daniel, "A mixed-reality system for breast surgical planning," in *2017 IEEE International Symposium on Mixed and Augmented Reality (ISMAR-Adjunct)*, 2017, pp. 269-274: IEEE.

[7] G. Yu, Y. Hu, and J. Dai, "Topotag: A robust and scalable topological fiducial marker system," *IEEE transactions on visualization and computer graphics,* vol. 27, no. 9, pp. 3769-3780, 2020.

[8] C. Inc. (2022, March 21, 2022). *MicronTracker Specifications.* Available: https://www.claronav.com/microntracker/microntracker-specifications/

[9] M. Kalaitzakis, B. Cain, S. Carroll, A. Ambrosi, C. Whitehead, and N. Vitzilaios, "Fiducial Markers for Pose Estimation," *Journal of Intelligent & Robotic Systems,* vol. 101, no. 4, p. 71, 2021/03/26 2021.

[10] M. B. Yaldiz, A. Meuleman, H. Jang, H. Ha, and M. H. Kim, "DeepFormableTag: end-to-end generation and recognition of deformable fiducial markers," *ACM Transactions on Graphics (TOG),* vol. 40, no. 4, pp. 1-14, 2021.

[11] E. Cheang, R. Ha, C. M. Thornton, and V. L. Mango, "Innovations in image-guided preoperative breast lesion localization," *The British Journal of Radiology,* vol. 91, no. 1085, p. 20170740, 2018.

[12] G. Franceschini *et al.*, "Image-guided localization techniques for surgical excision of non-palpable breast lesions: an overview of current literature and our experience with preoperative skin tattoo," *Journal of Personalized Medicine,* vol. 11, no. 2, p. 99, 2021.

[13] K. Kaczmarski *et al.*, "Surgeon re-excision rates after breast-conserving surgery: a measure of low-value care," *Journal of the American College of Surgeons,* vol. 228, no. 4, pp. 504-512. e2, 2019.

[14] M. A. Mallory *et al.*, "Feasibility of Intraoperative Breast MRI and the Role of Prone Versus Supine Positioning in Surgical Planning for Breast-Conserving Surgery," *The Breast Journal,* vol. 23, no. 6, pp. 713-717, Nov 2017.

[15] E. C. Gombos *et al.*, "Intraoperative supine breast MR imaging to quantify tumor deformation and detection of residual breast cancer: preliminary results," *Radiology,* vol. 281, no. 3, pp. 720-729, 2016.

[16] H. Satake, S. Ishigaki, M. Kitano, and S. Naganawa, "Prediction of prone-to-supine tumor displacement in the breast using patient position change: investigation with prone MRI and supine CT," *Breast Cancer,* vol. 23, no. 1, pp. 149-158, 2016.

[17] L. A. Carbonaro, P. Tannaphai, R. M. Trimboli, N. Verardi, M. P. Fedeli, and F. Sardanelli, "Contrast enhanced breast MRI: spatial displacement from prone to supine patient's position. Preliminary results," *European journal of radiology,* vol. 81, no. 6, pp. e771-e774, 2012.

[18] R. H. Conley *et al.*, "Realization of a biomechanical model-assisted image guidance system for breast cancer surgery using supine MRI," (in English), *International Journal of Computer Assisted Radiology and Surgery,* Article vol. 10, no. 12, pp. 1985-1996, Dec 2015.

[19] R. J. Barth *et al.*, "A Randomized Prospective Trial of Supine MRI-Guided Versus Wire-Localized Lumpectomy for Breast Cancer," *Annals of Surgical Oncology,* pp. 1-10, 2019.

[20] Y. Yang *et al.*, "An intraoperative measurement method of breast symmetry using three-dimensional scanning technique in reduction mammaplasty," *Aesthetic Plastic Surgery,* vol. 45, no. 5, pp. 2135-2145, 2021.

[21] K. C. Koban, F. Härtnagl, V. Titze, T. L. Schenck, and R. E. Giunta, "Chances and limitations of a low-cost mobile 3D scanner for breast imaging in comparison to an established 3D photogrammetric system," *Journal of Plastic, Reconstructive & Aesthetic Surgery,* vol. 71, no. 10, pp. 1417-1423, 2018.

[22] G. Ruiz, E. Ramon, J. García, F. M. Sukno, and M. A. G. Ballester, "Weighted regularized statistical shape space projection for breast 3D model reconstruction," *Medical Image Analysis,* vol. 47, pp. 164-179, 2018.

[23] A. Mazier, S. Ribes, B. Gilles, and S. P. Bordas, "A rigged model of the breast for preoperative surgical planning," *Journal of Biomechanics,* vol. 128, p. 110645, 2021.

[24] M. W. Göpper, J. Neubauer, Z. Kalash, G. B. Stark, and F. Simunovic, "Improved accuracy of breast volume calculation from 3D surface imaging data using statistical shape models," *PloS one,* vol. 15, no. 11, p. e0233586, 2020.

[25] M. J. Pallone, S. P. Poplack, H. B. Avutu, K. D. Paulsen, and R. J. Barth, Jr., "Supine breast MRI and 3D optical scanning: a novel approach to improve tumor localization for breast conserving surgery," *Annals of Surgical Oncology,* vol. 21, no. 7, pp. 2203-8, Jul 2014.

[26] M. Sakakibara *et al.*, "Breast-Conserving Surgery Using Projection and Reproduction Techniques of Surgical-Position Breast MRI in Patients with Ductal Carcinoma In Situ of the Breast," *Journal of the American College of Surgeons,* vol. 207, no. 1, pp. 62-68, 2008/07/01/ 2008.

[27] R. Nakamura *et al.*, "Breast-conserving surgery using supine magnetic resonance imaging in breast cancer patients receiving neoadjuvant chemotherapy," *The Breast,* vol. 17, no. 3, pp. 245-251, 2008.

[28] Z.-Y. Wu *et al.*, "Breast-conserving surgery with 3D-printed surgical guide: a single-center, prospective clinical study," *Scientific Reports,* vol. 11, no. 1, pp. 1-8, 2021.

[29] B. S. Ko *et al.*, "MRI-based 3D-printed surgical guides for breast cancer patients who received neoadjuvant chemotherapy," *Scientific Reports,* vol. 9, no. 1, pp. 1-6, 2019.

[30] R. J. Barth *et al.*, "A patient-specific 3D-printed form accurately transfers supine MRI-derived tumor localization information to guide breast-conserving surgery," *Annals of surgical oncology,* vol. 24, no. 10, pp. 2950-2956, 2017.

[31] M. Ebrahimi, P. Siegler, A. Modhafar, C. M. Holloway, D. B. Plewes, and A. L. Martel, "Using surface markers for MRI guided breast conserving surgery: a feasibility survey," *Phys Med Biol,* vol. 59, no. 7, pp. 1589-605, Apr 7 2014.

[32] S. L. Perkins, M. A. Lin, S. Srinivasan, A. J. Wheeler, B. A. Hargreaves, and B. L. Daniel, "Perceptual accuracy of a mixed-reality system for MR-guided breast surgical planning in the operating room," in *Proceedings of the 26th Annual Meeting of the ISMRM, Paris, France,* 2018, p. 607.

[33] W. L. Richey, J. S. Heiselman, M. Luo, I. M. Meszoely, and M. I. Miga, "Impact of deformation on a supine-positioned image guided breast surgery approach," *International Journal of Computer Assisted Radiology and Surgery,* Journal vol. 16, no. 11, p. 2055—2066, 2021.

[34] R. E. Ong, J. J. Ou, and M. I. Miga, "Non-rigid registration of breast surfaces using the laplace and diffusion equations," *Biomedical Engineering Online,* vol. 9, no. 1, p. 8, 2010.

[35] W. L. Richey, J. S. Heiselman, M. J. Ringel, I. M. Meszoely, and M. I. Miga, "Computational Imaging to Compensate for Soft-Tissue Deformations in Image-Guided Breast Conserving Surgery," *IEEE Transactions on Biomedical Engineering,* 2022.

[36] A. L. Simpson *et al.*, "Comparison study of intraoperative surface acquisition methods for surgical navigation," *IEEE Transactions on Biomedical Engineering,* vol. 60, no. 4, pp. 1090-1099, 2012.

[37] Z. Zhang, "A flexible new technique for camera calibration," *IEEE Transactions on pattern analysis and machine intelligence,* vol. 22, no. 11, pp. 1330-1334, 2000.

[38] "Computer Vision Toolbox," ed. Natick, Massachusets, United States: The Mathworks Inc., 2019.

[39] D. Bradley and G. Roth, "Adaptive thresholding using the integral image," *Journal of graphics tools,* vol. 12, no. 2, pp. 13-21, 2007.

[40] P. F. Alcantarilla, A. Bartoli, and A. J. Davison, "KAZE features," in *European conference on computer vision*, 2012, pp. 214-227: Springer.

[41] N. D. I. (2020, June 2 2021). *Polaris Vicra - NDI.* Available: https://www.ndigital.com/products/polaris-vicra/

[42] K. S. Arun, T. S. Huang, and S. D. Blostein, "Least-squares fitting of two 3-D point sets," *IEEE Transactions on pattern analysis and machine intelligence,* no. 5, pp. 698-700, 1987.

[43] J. M. Fitzpatrick, J. B. West, and C. R. Maurer, "Predicting error in rigid-body point-based registration," *IEEE Transactions on Medical Imaging,* vol. 17, no. 5, pp. 694-702, 1998.

[44] H. Sarmadi, R. Muñoz-Salinas, M. Á. Berbís, A. Luna, and R. Medina-Carnicer, "Joint scene and object tracking for cost-Effective augmented reality guided patient positioning in radiation therapy," *Computer Methods and Programs in Biomedicine,* vol. 209, p. 106296, 2021.

[45] W. L. Richey, J. Heiselman, M. Luo, I. M. Meszoely, and M. I. Miga, "Textual fiducial detection in breast conserving surgery for a near-real time image guidance system," in *Medical Imaging 2020: Image-Guided Procedures, Robotic Interventions, and Modeling*, 2020, vol. 11315, p. 113151L: International Society for Optics and Photonics.

[46] P. F. Alcantarilla, J. Nuevo, and A. Bartoli, "Fast Explicit Diffusion for Accelerated Features in Nonlinear Scale Spaces," in *Proceedings of the British Machine Vision Conference 2013*, 2013, pp. 13.1-13.11: British Machine Vision Association.

[47] B. Ramkumar, R. Laber, H. Bojinov, and R. S. Hegde, "GPU acceleration of the KAZE image feature extraction algorithm," *Journal of Real-Time Image Processing,* vol. 17, no. 5, pp. 1169-1182, 2020.